Chain Folding Produces a Multilayered Morphology in a Precise Polymer: Simulations and Experiments

Edward B. Trigg,[†] Mark J. Stevens,[‡] and Karen I. Winey[*,†]

[†]Department of Materials Science and Engineering, University of Pennsylvania, Philadelphia, Pennsylvania 19104, United States
[‡]Center for Integrated Nanotechnologies, Sandia National Laboratories, Albuquerque, New Mexico 87185, United States

S *Supporting Information*

ABSTRACT: Precise control over polymer architecture unlocks the potential for engineered self-assembled crystal structures with useful features on the nanometer length scale. Here we elucidate the structure of the ordered phase of a semicrystalline, functional polyethylene having a precise linear architecture, namely, pendant carboxylic acid groups precisely every 21st backbone carbon atom. By comparing the results of atomistic molecular dynamics simulations with experimental X-ray scattering and Raman spectroscopy data, we find that the polymer chains are folded in a hairpin manner near each carboxylic acid group, giving rise to multiple embedded layers of functional groups that have an interlayer distance of 2.5 nm. This is in contrast to other precise polyethylenes, where the chains are mostly trans within the crystals. Such layers could act as two-dimensional pathways for ionic or molecular transport given an appropriate choice of functional group.
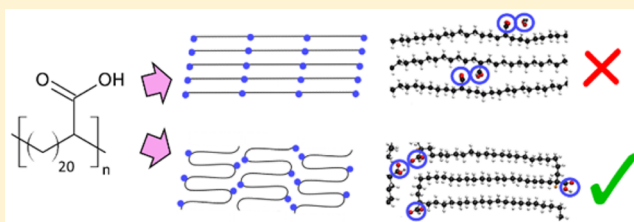
1. INTRODUCTION

Controlling polymer structure to produce desired material properties is a fundamental challenge in polymer chemistry. Recent advances have synthesized linear polymers with precisely placed associating side groups (termed *precise polymers*), enabling control of the polymer crystal structure and the location of the functional groups therein.[1−3] Perhaps a continuous network of acidic or charged side groups within a crystal structure would act as a pathway for efficient ionic, protonic, or molecular transport *through* crystalline regions of the polymer and thereby have major implications for membrane technology.[4] Here we demonstrate that a new chain-folded structure can be achieved simply by precise placement of acid groups along linear polyethylene (PE). The resulting layers of acid groups may provide a new route to effective transport within polymeric crystals.

Ionomers, or polymers with a covalently bound ionic species, are of current interest as ion-conducting membranes for use as electrolytes in electrochemical energy storage devices[5−7] because of several attractive properties, including nonflammability,[8] chemical stability leading to improved device lifetime,[9] and single-ion conduction.[10] However, the ion conductivity in ionomers, which are typically amorphous, remains too low for practical use. Research on ion conduction in semicrystalline polymer systems has been less widespread, despite some promising results with poly(ethylene oxide)-based systems.[11−13] A single-ion-conducting self-assembled monolayer with high conductivity, composed of densely packed carboxyl-terminated silanes, was recently reported,[4] demonstrating that densely packed layers of acid groups could be an effective strategy for producing high ion conductivity. In the present

study, we aim to translate this strategy to a semicrystalline polymer system. We investigate the crystal structure of a precise linear PE with stereoirregular carboxylic acid groups bonded to every 21st carbon atom along the backbone, termed p21AA. This structure contains dense layers of hydrogen-bonded COOH groups that may provide efficient pathways for ion transport, similar to the self-assembled monolayer.

Acyclic diene metathesis (ADMET) polymerization has produced linear PEs with precisely spaced side groups (e.g., bonded to every 21st carbon atom).[2,14,15] Studies of these materials have proven that precise architectures control the crystal structure and crystallite size with superior precision.[1,3,16−21] In ADMET-synthesized precisely functionalized PEs, two distinct types of crystals have been reported in detail. The first are *thin crystals* (Figure 1a), in which the crystal thickness spans only one alkyl segment. In this case the functional groups are excluded from the crystal. This morphology has been observed in polymers with nonpolar functional groups that are too large to be accommodated into the crystal, including ADMET polymers with hexyl branches every 21st backbone carbon,[22] butyl branches every 39th backbone carbon,[23] and others.[24]

In the second type of crystal, *extended-chain crystals*, the functional groups are small enough to be embedded inside the crystalline regions (Figure 1b), and these functional groups arrange into layers to optimize the packing. To accommodate the extra bulk of the functional groups, the crystalline packing of alkyl segments in these crystals is typically different from the
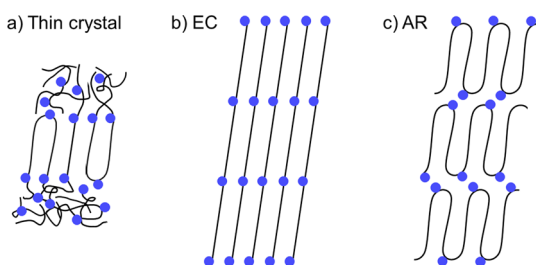
Figure 1. Three possible types of layered crystals formed by precise polyethylenes. Black lines represent alkyl backbones, and blue circles represent functional groups. In thin crystals (a), which are bounded by amorphous regions when crystallized from the melt, the crystal thickness spans only one alkyl segment, while in extended-chain (EC) (b) and adjacent-reentry (AR) (c) crystals, the crystal thickness is not limited to one segment. In (b) and (c), amorphous regions also exist but are not shown. All three types contain functional group layers.

orthorhombic structure of pure polyethylene, and the stems are often tilted with respect to the normal of the functional group layer. Aliphatic polyamides (nylons) are classic examples of precise polymers that form extended-chain layered crystallites.[25,26] In ADMET polyethylenes containing Cl or Br groups, a polymorphism of crystal structures was reported, all of which were of the extended-chain variety.[27,28] Methyl groups[16] and sulfone groups[29] also give rise to extended-chain crystals. In extended-chain crystals, the overall stem trajectory is similar to that in crystalline PE, although kinks in the chain backbone caused by gauche conformations near the functional groups have been observed in some halogen-containing precise polyethylenes.[28]

A third type of crystal, *adjacent-reentry crystals* (Figure 1c), is possible, though it has not been reported in ADMET polymers. Multilayer chain-folded structures related to Figure 1c have been demonstrated in other synthetic polymers. Recently, Ramakrishnan and co-workers reported such a morphology in polyesters containing alkyl segments in the backbone with precisely defined lengths, in which short poly(ethylene glycol) (PEG) chains were grafted to the polymer near each ester group.[30,31] The chain folds occurred near the grafting points, and the 20-carbon-long alkyl segments crystallized upon chain folding.

In the present study, we investigate the crystal structure of p21AA with respect to the three crystal types shown in Figure 1. Using atomistic molecular dynamics (MD) simulations,

X-ray scattering, and Raman spectroscopy, we find that neither the thin-crystal model nor the extended-chain model accurately matches the experimental data for semicrystalline p21AA. Meanwhile, the multilayer adjacent-reentry structure (Figure 1c), wherein the polymer chains make hairpin turns near each functional group, matches the experimental data very well. This morphology type is particularly interesting because the layers of functional groups are free of polymer backbones and large functional groups may be accommodated. With an appropriate choice of functional group, this morphology may be useful for applications such as transport of ions, protons or small molecules through the layers containing the functional groups.

2. METHODS

A detailed description of the experimental and simulation methods can be found in the Supporting Information.

2.1. Initial Structures for Simulations. All of the p21AA molecules consisted of four monomers, i.e., 84 backbone carbon atoms with pendant COOH groups on the 11th, 32nd, 53rd, and 74th carbons.

p21AA Extended Chain. All of the initial structures of the extended-chain (EC) type contained 70 molecules and were built using molecules with all-trans backbones. The initial lattice parameters were larger than those of typical crystalline PE to ensure that the COOH groups did not overlap with atoms belonging to neighboring chains, and this resulted in a low-density initial structure that densified upon relaxation via MD. Four EC simulations each with different starting conditions were carried out (Table 1). The initial structure of EC1 used stereoregular molecules with OCOH dihedrals in trans conformations, and the chains were packed with alternating backbone zigzag directions as found in orthorhombic PE but with expanded lattice parameters ($a = 10$ Å, $b = 7$ Å). The vector normal to the layer of COOH groups was tilted relative to the chain backbone, resulting in an overall monoclinic unit cell. EC2 was similar to EC1 but used stereoirregular molecules. EC3 used stereoregular molecules with OCOH dihedrals in cis conformations, and the molecules were arranged such that all of the COOH groups were paired into H-bonded dimers. This dimerization necessitated a different kind of chain packing in which all of the backbone zigzag directions were uniform. In the EC3 initial structure, the vector normal to the COOH layer was parallel to the chain backbone. EC4 was similar to EC3, but the COOH layer was tilted in an attempt to improve the packing of COOH groups in the initial structure.

p21AA Adjacent Reentry. All of the initial structures of the adjacent-reentry (AR) type used 96 molecules with $[110]_{\text{orthorhombic PE}}$ hairpin chain folds near each pendant acid group. The molecules were arranged so that neighboring alkyl segments had alternating zigzag directions, similar to orthorhombic PE. Four AR simulations were

Table 1. Simulations Performed

name	tacticity	initial ϕ_{OCOH}[a]	initial layer tilt	final energy [kJ/mol][b]	% gauche[c]	area per alkyl segment [Å²][d]
EC1	isotactic	trans	nonzero	−62	0.8	18.7
EC2	atactic	trans	nonzero	−25	15	20.2
EC3	isotactic	cis	zero	−18		
EC4	isotactic	cis	nonzero	−61[e]		
AR1	syndiotactic	cis	nonzero	−30	24	19.9
AR2	atactic	cis	nonzero	−12	27	21.2
AR3	syndiotactic	trans	zero	−9		
AR4	syndiotactic	trans	nonzero	−21		
AM	syndiotactic	−	−	0	35[f]	
PE	−	−	−	−	0.0	18.0

[a]OCOH dihedral angles were initially all trans or all cis. [b]Final potential energy per mole of repeat unit (i.e., 21 backbone carbons) at 348 K, relative to the amorphous state. [c]Final percentage of C−C−C−C backbone dihedral angles that are gauche at 298 K. Only the middle two monomers of each molecule are counted. Dihedrals are considered gauche when $\phi < 120°$ or $\phi > 240°$. [d]At 298 K (from final structure). Error: ±1 Å². [e]The final energies of EC4 and EC1 are very similar because their final structures are very similar despite different initial conditions. [f]At 348 K.

carried out, with four distinct initial structures. In the simplest case, AR3, molecules containing the hairpin folds described above were placed on a nearly orthorhombic lattice. A slight departure from orthorhombicity was required by the presence of chain ends within the structure, as two neighboring CH_3 groups require more volume than two CH_2 groups that are bonded together. The plane containing the COOH layers was thus nearly orthogonal to the trans alkyl segment axes. OCOH dihedrals were initially in trans conformations, and the molecules were stereoregular. AR4 was similar to AR3 except that a significant initial tilt was introduced into the COOH layers such that they were far from orthogonal to the alkyl stems. AR1 was similar to AR4, except that the OCOH dihedrals were initially in cis conformations instead of trans ones. AR2 was similar to AR1, but the molecules were stereoirregular.

2.2. Structural Relaxation via Molecular Dynamics. All of the EC and AR p21AA simulations were treated in the following manner: local energy minimization, relaxation at 273 K for 1 ns, heating to 348 K at 10 K/ns, and relaxation at 348 K for the amount of time indicated in Table S1. Then EC1, EC2, AR1, and AR2 were cooled to 298 K at 100 K/ns and relaxed at 298 K for 15 ns for direct comparison to experimental data. These results at 298 K are shown in Figures 3, 5, 6, 7, 9, and S5 and the two right-most columns of Table 1. The simulation results shown in Figures 4 and 8 are at 348 K, but little change was observed upon cooling to 298 K in the simulations that were cooled. It should be noted that the temperature of structural relaxation in the simulations of crystalline p21AA (348 K) is above the experimental melting temperature (319 K). However, 348 K was required in order to obtain sufficient mobility to relax the structures, as the dynamics were relatively slow because of hydrogen bonding.

3. RESULTS AND DISCUSSION

First we show that the thin-crystal model does not fit the experimental data. The structures from the extended-chain and adjacent-reentry models as determined by the MD simulations are presented next. These simulation data are then compared to experimental X-ray and Raman data, which match the results of the AR simulations.

3.1. Number of Layers in a Crystallite. To assess the viability of the thin-crystal model (Figure 1a) for p21AA, the Scherrer equation is applied to synchrotron-source X-ray scattering of melt-crystallized p21AA (Figure 2). A series of
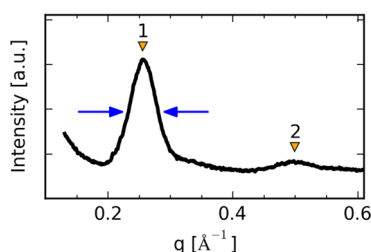

Figure 2. Synchrotron X-ray scattering at 298 K of p21AA crystallized from the melt.

peaks in the ratio 1:2:3 is observed in p21AA, corresponding to layers of COOH groups with an interlayer spacing of 25 Å, as reported previously.[3,20,21] The Scherrer equation relates the full width at half-maximum (fwhm) of the first peak to the approximate lower limit of the correlation length along the layer normal: $l_{correlation} \geq \frac{2\pi}{\Delta q}$, where Δq is the fwhm. This analysis yields a minimum correlation length of 130 Å, corresponding to five COOH layers. Thus, the average crystallite contains at least five layers, so the thin-crystal model, which contains only two layers, can be ruled out. It should be noted that bulk-crystallized p21AA was previously

found to be semicrystalline on the basis of the existence of a small-angle X-ray scattering peak at 0.038 Å^{-1}, corresponding to an intercrystallite distance of ∼160 Å.[3]

3.2. Simulated Extended-Chain Structures. The extended-chain structures (stereoregular, EC1, and stereoirregular, EC2) are summarized visually in Figures 3 and 5. The initial structures for the EC simulations were constructed with the backbones in all-trans (extended) conformations (Figure 3a) and contained 70 molecules, each consisting of four monomers. Figure 3c shows the full simulation box of the final EC1 simulation. Three projections of each final simulation box are shown in Figure S1. Two additional stereoregular simulations, EC3 and EC4, are summarized visually in Figures S2 and S3.

In EC1, the stereoregular molecules form a nearly defect-free crystal structure, as shown in Figure 3b,d,e, in which xz, xy, and yz slices or projections, respectively, are presented. Carboxylic acid groups H-bond with each other in the trans/multimer motif (see Figure 4a) to form infinite chains (or columns) along the y axis. These infinite columns of acid groups exist in pairs, and these pairs are distributed periodically among the alkyl regions. Each column is highlighted in purple in Figure 3b,e. Figure 3 conveys the high degree of ordering in this simulation, with ∼97% of the COOH groups participating in trans/multimer H-bonding (see Figure 4b) at any point in time after initial relaxation.

The alkyl segments are also highly ordered and more than 99% trans. In Figure 3d, the backbone axis is into the page, and the zigzag direction of each backbone is indicated by a green arrow. It is clear that the zigzag direction is nearly uniform across all of the chains. Therefore, this structure is quite distinct from orthorhombic PE and bears more resemblance to monoclinic or triclinic PE. There is some long-range curvature to the backbones, as is apparent in Figure 3b, to allow for efficient packing of the COOH columns. This curvature is achieved by deviations of the backbone dihedral angles from the exact trans value (180°) by as much as 10° while still remaining within the trans potential well (Figure S5 shows a substantially broader distribution of trans dihedral angles in EC1 than in PE). Remarkably, the acid groups can be accommodated in this structure without significant introduction of backbone gauche conformations. A single defect—a pair of backbone gauche conformations—can be found in Figure 3b, highlighted by the blue circle.

EC1 has by far the lowest final potential energy of any structure studied (Table 1), consistent with the very high degree of ordering seen in Figures 3 and 4b. (The energy of EC4 is similar to that of EC1 because the final structures are very similar.) This low energy arises primarily because more than 99% of the backbone conformations are trans, 99% of the available hydrogen bonds are satisfied, and the packing is efficient. However, EC1 is not comparable to the experimentally observed polymer, which is stereoirregular.

Figure 5 presents the final structure obtained from EC2, the extended-chain simulation of stereoirregular molecules. Clearly, the lack of stereoregularity greatly increases the degree of disorder compared with EC1, and the potential energy is correspondingly much higher (Table 1). As can be seen in Figure 5a,c, the positions of the COOH groups, highlighted by the purple ovals, are irregular and lack periodic ordering. The percentage of backbone gauche conformers increases from less than 1% in EC1 to 15% in EC2 (Table 1; the gauche conformers are indicated with blue circles in Figure 5), and the
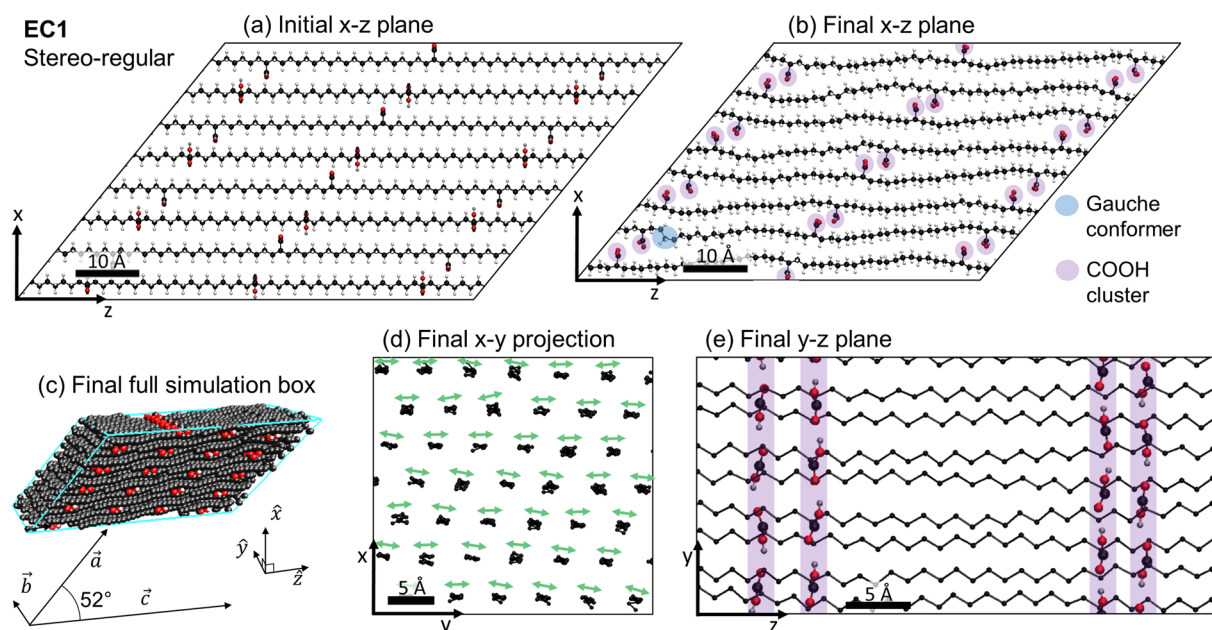
Figure 3. Snapshots from the EC1 simulation: (a) *xz* plane of the initial configuration; (b) *xz* plane of the final configuration; (c) full simulation box of the final configuration with simulation box edges $\vec{a}$, $\vec{b}$, and $\vec{c}$ and orthogonal coordinate system $\hat{x}$, $\hat{y}$, and $\hat{z}$ defined; (d) *xy* projection of the final configuration (chain axis into the page) with only methylene carbons visible; (e) *yz* plane of the final configuration with alkyl hydrogens not shown. All of the atoms are shown in (a−c). Carbon atoms are shown in black, oxygen atoms in red, and hydrogen atoms in gray. Green arrows in (d) indicate the zigzag directions of the all-trans backbones. The temperature in (b−e) is 298 K.

intramolecular component of the potential energy is 18 kJ/mol higher than in EC1 as a result (Table S1). The strong driving force for H-bonding causes H-bonds to form at the expense of some backbone order. Figure 5b shows that the backbone zigzag directions are somewhat disordered, in some regions resembling the packing in triclinic or monoclinic PE and in other regions resembling orthorhombic PE packing. The regions of orthorhombic-PE-like packing could be influenced by the initial configuration, which was 100% orthorhombic. Trans/multimer H-bonding is still the most common H-bonding type, but only ~37% of COOH groups are found in this state, and only 82% of the available H-bonds are satisfied (Figure 4c). Nearly one-third of the COOH groups have only one H-bond, a clear indication of a lack of favorable packing. The stereoirregularity greatly disrupts the ability to H-bond and pack efficiently, significantly increasing the number of backbone gauche conformations and the potential energy of the extended-chain structure.

3.3. Simulated Adjacent-Reentry Structures. The adjacent-reentry structures, stereoregular (AR1) and stereo-irregular (AR2), are shown in Figures 6 and 7. The initial structures for the AR simulations were constructed with a hairpin chain fold at the location of each COOH group (Figure 6a). The image shows the structure before densification, and thus, the gap between acid layers is large. The full simulation box of the final configuration of AR1 is shown in Figure 6c. Three projections of each simulation box are shown in Figure S6. The additional stereoregular simulations, AR3 and AR4, are summarized visually in Figures S7 and S8.

Representative slices and projections of the final structure of AR1 are shown in Figure 6b,d,e. The COOH groups are located on the "corners" of the chain folds (Figure 6b), and they usually H-bond with the COOH group on the corner of the opposing fold (highlighted by purple ovals). The H-bonding type is predominantly cis/multimer, meaning that the

OCOH dihedral angles are cis and each COOH group is H-bonded to two different partners (see Figure 4a). Figure 4d shows this clearly, where roughly 75% of the COOH groups are cis/multimer. Overall, 96% of the available H-bonds are satisfied. Alkyl segments are mostly trans except for the portions participating in chain folds, with four to five gauche conformations associated with a typical chain fold. In Figure 6d, which shows only the mostly trans alkyl segments and not the chain folds or COOH groups, the zigzag directions of the backbones can be seen. As in EC1, the zigzag directions of the alkyl segments are generally uniform, although several defective segments with other zigzag directions are present. Figure 6c shows that the plane containing the COOH groups is not orthogonal to the chain axis of the trans backbones, although the tilt is not quite as severe as in the EC simulations (Figures 3c and 5a).

Overall, the structure of AR1 is more disordered than that of EC1. This may be at least partially explained by the presence of chain ends within the crystal structure (chain end locations are indicated with orange circles in Figure 6a,b,d). In EC1, the chain ends are segregated to the sides of the simulation box, but constructing AR1 that way was not possible. The potential energy of AR1 is much higher than that of EC1, largely because of the many gauche conformations in the chain folds. The Coulombic contribution to the potential energy is lower in AR1 than in EC1 (Table S1), perhaps as a result of the greater segregation of COOH groups from alkyl segments in AR1.

Figure 7 shows AR2, the stereoirregular adjacent-reentry structure. The stereoirregularity clearly disrupts the ordering of the H-bonding compared with AR1. The percentage of potential H-bonds satisfied is 82%, which is identical to that in EC2 and much lower than that in either AR1 or EC1. Both AR2 and EC2 possess a mixture of states of COOH groups, predominantly trans/multimer, cis/multimer, and one H-bond (Figure 4e). Figure 7a,c shows that the H-bonding is quite
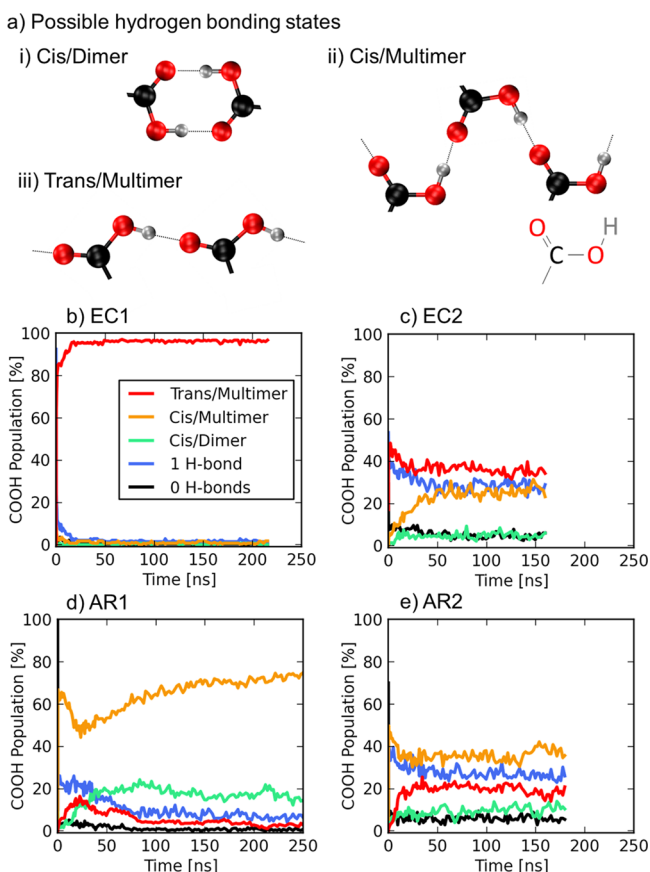
Figure 4. (a) Possible COOH H-bonding states and their nomenclature. (b–e) Percentages of COOH groups in various H-bonding states over time in (b) EC1, (c) EC2, (d) AR1, and (e) AR2. "Cis" and "Trans" refer to the OCOH dihedral conformation. "Dimer" refers to a COOH group that is H-bonded twice to the same partner, while "Multimer" refers to a COOH group that has two H-bonds to two different partner COOH groups. Data are for 343 K; the change after cooling to 298 K was less than 5% for the simulations that were cooled.

Figure 5. Snapshots from the EC2 simulation: (a) *xz* plane of the final configuration; (b) *xy* projection of the final configuration (chain axis into the page); (c) *yz* plane of the final configuration. The *x*, *y*, and *z* directions are defined in Figure 3. It should be noted that some COOH groups are H-bonded to COOH groups that are hidden from view in (a) and (c). All of the atoms are shown in (a); only backbone carbon atoms are shown in (b), and only backbone carbons and COOH groups are shown in (c). The temperature is 298 K.

disordered and aperiodic. In Figure 7b, the zigzag directions of the alkyl segments are quite disordered while still maintaining mostly trans conformations. The packing of alkyl segments appears to be roughly hexagonal, reminiscent of the hexagonal rotator phase of *n*-alkanes.[32] The potential energy of AR2 is significantly higher than that of EC2 (Table 1), and this energetic difference is entirely due to the difference in intramolecular energy (Table S1), which is a consequence of chain folding in AR2.

3.4. Layer Spacing. The distance between layers of COOH groups is observable experimentally via X-ray scattering and is therefore of critical importance in comparing the simulated structures with experiment. Remarkably, we find excellent agreement between *all* of the adjacent-reentry simulations (AR1, AR2, AR3, and AR4) and the experimental value of 25 Å (Figure 8). The stereoregularity does not have a significant effect on the layer spacing (AR1 vs AR2). In addition, the initial angle between the alkyl segment axis and the vector normal to the acid layer plane was 0° in AR3, and the layer spacing of the final structure did not change significantly compared with that in AR1 because the angle became nonzero during relaxation. The initial OCOH dihedral angle also did not significantly affect the layer spacing (AR1 vs AR4). The robustness of the
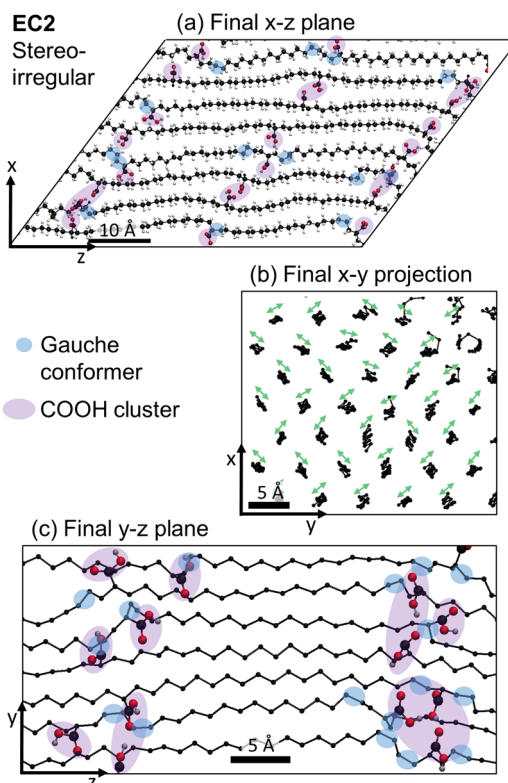
agreement between simulation and experiment suggests that the adjacent-reentry structure is a reasonable model for the experimentally observed structure of p21AA crystallized from the melt.

On the other hand, the layer spacings in the four extended-chain simulations (EC1, EC2, EC3, and EC4) are significantly lower than the experimentally observed spacing. The layer spacings of both EC1 and EC2 are ~20.5 Å, which is almost 20% lower than the experimental value. Although the all-trans (extended) length of the monomeric unit is 26.7 Å, the layer spacing is much lower than this in EC1 and EC2 because the backbone axis is far from orthogonal to the plane containing the COOH groups. In EC3, the backbone axis *was* orthogonal to the COOH layer plane in the initial structure but quickly became nonorthogonal during relaxation, and the layer spacing decreased from ~26.7 to 21 Å. The COOH layer must be nonorthogonal to the backbone axis in the extended-chain structure for efficient packing. In EC4, a rapid increase in layer spacing is observed after ~30–40 ns at 348 K. This rapid increase is due to a transition of the OCOH dihedral angles from cis to trans (Figure S4b), and after 40 ns the structure resembles EC1 but with a stacking fault (Figure S3d). On the basis of these simulations, the nonorthogonality required in extended-chain structures causes the layer spacing to be less than 22 Å. As a result, we conclude that these extended-chain structures are unlikely to be the dominant conformation type in the bulk p21AA studied experimentally.
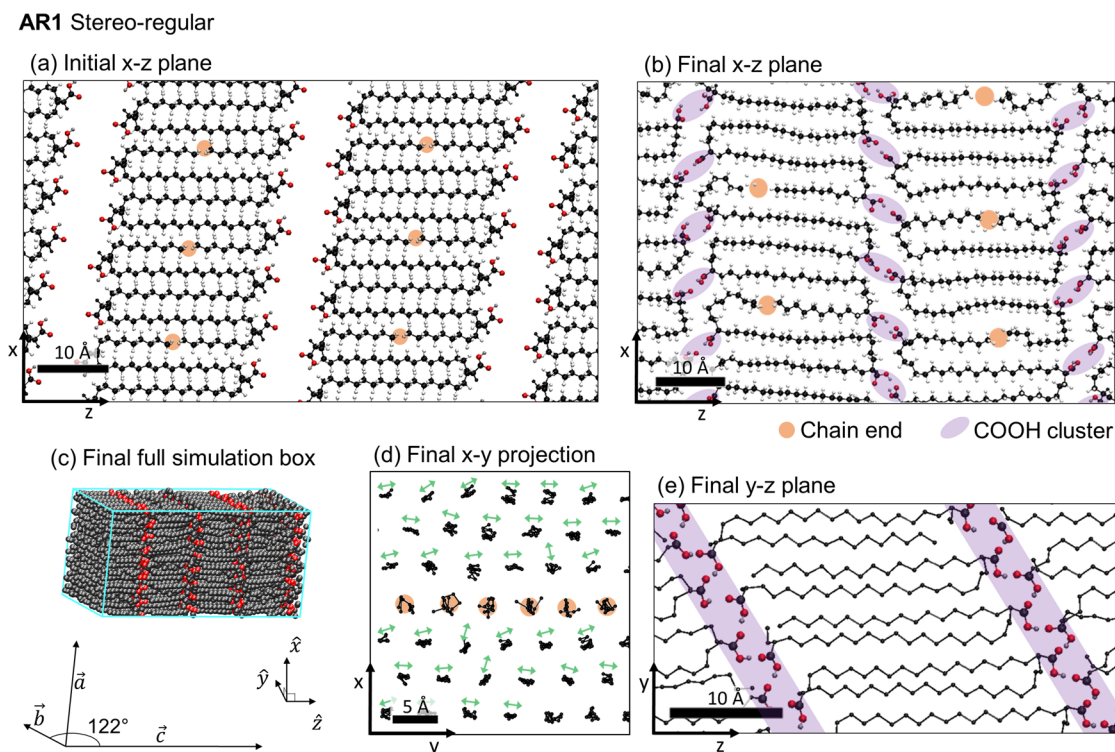
AR1 Stereo-regular

Figure 6. Snapshots from the AR1 simulation: (a) xz plane of the initial configuration; (b) xz plane of the final configuration; (c) full simulation box of the final configuration with the simulation box edges $\vec{a}$, $\vec{b}$, and $\vec{c}$ and the orthogonal coordinate system $\hat{x}$, $\hat{y}$, and $\hat{z}$ defined; (d) xy projection of the final configuration (chain axis into the page); (e) yz plane of the final configuration. All of the atoms are shown in (a–c); only backbone carbon atoms are shown in (d), and only backbone carbons and COOH groups are shown in (e). The temperature is 298 K.

3.5. Local Packing of Alkyl Segments. Structure factors were calculated from the stereoirregular simulations, AR2 and EC2, at 298 K for comparison with experimental X-ray scattering from a bulk sample, and the comparison is shown in Figure 9. The experimental data can be decomposed into an amorphous halo (dashed gray) and a Bragg peak (solid gray). This Bragg peak is centered at 1.47 Å^{-1} and is reproduced behind the AR2 and EC2 curves in Figure 9 for comparison. The simulations are solely crystalline and do not possess the amorphous halo.

The structure factor of AR2 shows a single strong reflection in the range of 1 Å^{-1} < q < 2 Å^{-1}. This is consistent with a hexagonal arrangement of alkyl segments as observed in wide-angle X-ray scattering (WAXS) of PE in its high-pressure hexagonal phase.[33] The structure factor of AR2 is remarkably consistent with the experimental result (solid gray), as both consist of a single peak centered at 1.47 Å^{-1}. Meanwhile, the structure factor of EC2 shows multiple reflections, probably due to nonhexagonal packing of alkyl segments as seen in Figure 5b. The position of the most intense peak in the EC2 structure factor is 1.44 Å^{-1}, which is lower than the experimental value but comparable to the discrepancy observed in our PE simulation. It should be noted that the peak breadths of the simulation structure factors were chosen to best match experiment. The structure factor from our simulation of oligomeric PE (C84) (Figure S9) shows reasonable agreement with typical experimental X-ray scattering of PE (experimental q_{110} = 1.53 Å^{-1},[34] simulated q_{110} = 1.55 Å^{-1}).

To further characterize the packing of the alkyl segments, the Raman spectra of p21AA and HDPE were measured (Figure 10). Perhaps the most striking difference between the two spectra is in the CH$_2$ bend region (1400–1500 cm^{-1}). HDPE shows features typical of orthorhombic packing, specifically a sharp peak at 1415 cm^{-1} (Figure 10, red line), while the spectrum of p21AA entirely lacks this peak. Instead, the CH$_2$ bend region of p21AA strongly resembles that of hexagonal PE, having a somewhat broad feature centered at ~1440 cm^{-1}.[35] Overall, in a comparison of orthorhombic, monoclinic, triclinic, and hexagonal n-alkanes,[36] p21AA clearly resembles the hexagonal phase most strongly. On the basis of this analysis and the single Bragg peak observed in X-ray scattering that is consistent with the AR simulations, we conclude that the methylene segments of p21AA pack in a hexagonal fashion. Hexagonal packing was previously observed in two ADMET polyethylenes with methyl groups every 15 and 21 carbons.[16]

Thus, we assign the single sharp experimental X-ray scattering peak to the $[100]_{\text{hexagonal PE}}$ reflection. The experimental d_{100} of p21AA is 4.27 Å, which is 3% larger than that of hexagonal PE (4.13 Å);[33] this discrepancy is readily attributable to the very high pressures under which hexagonal PE was measured (>1500 bar). We conclude that the trans CH$_2$ segments in the ordered phase of p21AA are packed in a roughly hexagonal lattice and are most likely disordered with respect to rotation about their axes.

Shifting the focus to the C–C stretch region (1000–1200 cm^{-1}), the feature at 1083 cm^{-1} (Figure 10, gray line) is much more intense in p21AA than in HDPE. This feature is often assigned to amorphous backbone conformations,[35,37] while the adjacent sharp peaks at 1063 and 1130 correspond to backbone segments with at least 10 consecutive trans conformations.[38] The peaks at 1063 and 1130 cm^{-1} are broader in p21AA than in HDPE, perhaps indicating shorter consecutive trans segments in p21AA. The high intensity of the 1083 cm^{-1} feature in p21AA is consistent with lower crystallinity in p21AA than in
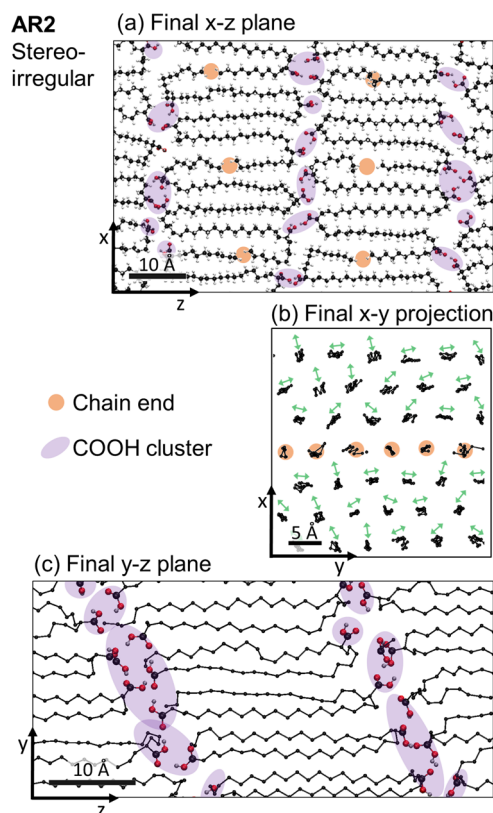
AR2
Stereo-irregular

(a) Final x-z plane

● Chain end

COOH cluster

(b) Final x-y projection

(c) Final y-z plane

Figure 7. Snapshots from the AR2 simulation: (a) *xz* plane of the final configuration; (b) *xy* projection of the final configuration (chain axis into the page) with only methylene carbons visible; (c) *yz* plane of the final configuration with alkyl hydrogens not shown. The *x*, *y*, and *z* directions are defined in Figure 6. It should be noted that some COOH groups are H-bonded to COOH groups that are hidden from view in (a) and (c). The temperature is 298 K.
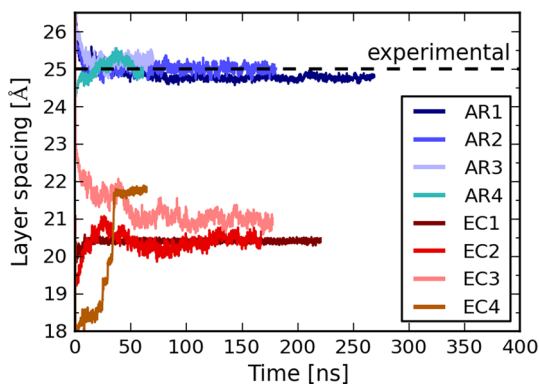
Figure 8. Layer spacings of adjacent-reentry and extended-chain simulations. The black dashed line shows the experimental layer spacing obtained from X-ray scattering of a bulk sample of p21AA at 298 K. All of the simulation data are for 348 K; the change upon cooling to 298 K is less than ±0.3 Å for simulations that were cooled.

HDPE, as reported previously by solid-state NMR spectroscopy (35%[21] and 44%[39] crystallinity have been reported for p21AA with different thermal histories). However, in crystalline C_{168} linear alkane, a feature at 1083 cm^{-1} was assigned to chain folding,[40] and the high intensity of the feature in p21AA could be indicative of chain folding within the crystal structure as in the adjacent-reentry simulations.
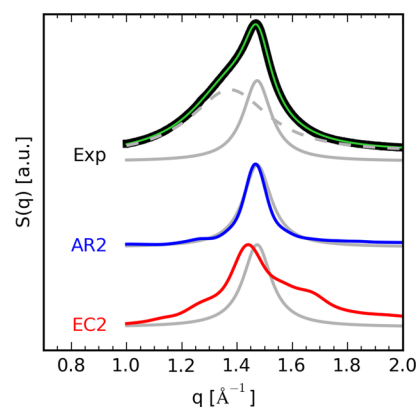

Figure 9. Comparisons of structure factors from simulations and experiment at 298 K. The experimental WAXS structure factor for semicrystalline p21AA (top) deconvoluted into amorphous and crystalline peaks (black, experimental; green, total fit; dashed gray, amorphous halo; solid gray, crystalline peak) and the structure factors calculated from the AR2 (middle) and EC2 (bottom) simulations are shown. The structure factor calculation yields a series of delta functions with defined relative intensities, and these delta functions were convoluted with Gaussian functions of uniform fwhm = 0.078 Å^{-1}, which was chosen to best match the experimental data.
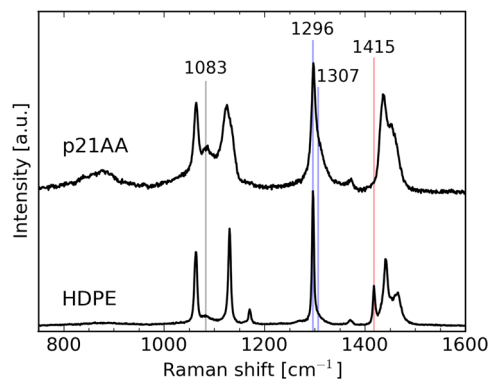

Figure 10. Raman spectrum of p21AA compared with that of HDPE at 298 K. The spectra have been vertically shifted and rescaled for clarity.

By examining the CH$_2$ twist region (1260−1360 cm^{-1}), Migler et al.[37] recently quantified the fraction of CH$_2$ units that belong to segments of at least three to five consecutive trans bonds, f_{trans}, in PE. This quantity was extracted from the ratio of the integrated intensities of the features at 1296 and 1307 cm^{-1} (Figure 10, blue lines).[37,41] Following this method, our value of f_{trans} in p21AA is 0.48, compared with 0.90 in HDPE (the fits are shown in Figure S10). This result should not be directly interpreted as the fraction of the crystalline phase in p21AA because gauche-rich chain folds within the ordered phase could contribute to the broad feature at 1307 cm^{-1}.

4. DISCUSSION

The agreement between the AR2 results and the experimental data is strong, but EC2 has a lower potential energy. This indicates that the kinetics of crystallization must also be considered. Melt-crystallized polymer systems are dynamically trapped in semicrystalline states, which are not in (or even near) the lowest-free-energy state. We expect this trapping to be even more pronounced when the polymer dynamics in the melt is significantly impeded by strongly interacting moieties, in

this case the H-bonding COOH groups. The question is when the crystallites form, which is more likely to occur, the extended-chain or adjacent-reentry structure? For crystallization to occur in p21AA, alkyl segments of neighboring chains must align such that their acid groups are in registry, requiring some degree of translational motion. However, if a chain folds at the location of a COOH group, the adjacent segments are already near the correct position to add to the growing crystal face. The unusual *multi*layered adjacent-reentry structure (Figure 1c) may be caused by H-bond templating. A chain-folded surface at the crystal−amorphous interface would be decorated with COOH groups that, through H-bonding with neighboring amorphous chains, could template the crystallization of those amorphous chains.

For a true thermodynamic comparison of the EC and AR simulations, the total free energy should be considered, not just the potential energy. Entropy was not measured in our simulations, as it is quite expensive to do so. Thus, the relative free energies of EC2 and AR2 are not known. The adjacent-reentry structure is likely to have higher entropy because of the conformational degrees of freedom arising from the chain folds and also the greater number of possible chain conformations (compared with a strictly straight backbone in the extended-chain case), which would imply a smaller entropic contribution to the free energy for the AR structure.

Several additional pieces of evidence point to the adjacent-reentry structure as the most likely. It is valuable to compare p21AA with two similar ADMET polymers, one with *two* carboxylic acid groups bonded to every 21st carbon (p21gAA) and the other with one phosphonic acid group bonded to every 21st carbon (p21PA).[21] Despite the very different van der Waals volumes of these three functionalities (approximately 35 $Å^3$ for COOH, 70 $Å^3$ for $(COOH)_2$, and 50 $Å^3$ for PO_3H_2),[42] the corresponding layer spacings vary by only 7%, and p21PA has the highest layer spacing of the three. If these were EC layers, a larger functional group volume would require a larger tilt angle between the normal to the functional group layer and the chain axes for efficient packing, thus decreasing the layer spacing, so we would expect p21PA to have a smaller layer spacing than p21AA because it has a larger van der Waals volume. Furthermore, p21AA, p21gAA, and p21PA show very similar primary melting points via differential scanning calorimetry (47.7, 46.1, and 47.4 °C, respectively),[21] and if their structures were EC, larger functional groups would be expected to perturb the crystal structure to a greater extent and lower the melting point. For example, changing the functional group from methyl to ethyl (each bonded to every 21st carbon) lowers the melting point from 63 to 24 °C.[24] Also, the melting points of p21AA, p21gAA, and p21PA are all within 4 °C of the melting points of chain-folded crystals of PEG-grafted polyesters with alkyl segment lengths of exactly 20,[30] further suggesting that the ADMET polymers have chain folding in their crystal structures.

While the adjacent-reentry model presented in this work agrees well with the experimental characterization of melt-crystallized p21AA, the morphology is likely more complex in reality. The chain folding is likely more irregular than constructed in the simulations or shown in Figure 1c, and a few extended chains might even exist as defects within the crystal. The simulations have only treated the structure of an infinite crystal composed of oligomeric molecules, and the larger-scale semicrystalline structure that incorporates a sizable amorphous fraction remains to be studied.

The intriguing consequence of finding layers of carboxyl groups within the AR crystal structure is the impact on transport of ions. The close proximity of the carboxyl groups as seen in Figure 7 could allow for ionic transport without extensive segmental motion of the polymer, which greatly impedes conduction. In this case, thermally activated ion hopping directly between carboxyl groups would dominate the transport mechanism. Such a phenomenon was recently reported in a carboxyl-terminated silane monolayer, in which Ag^+ and Ti^{4+} ions exhibited excellent conductivity across the surface of the self-assembled monolayer.[4] The high density of carboxyl groups at the surface, ~ 5 nm^{-2}, allowed the ions to move between sites. The areal density of carboxyl groups in a layer in our AR2 simulation is similar (4.3 nm^{-2}). These p21AA crystals therefore have the potential to provide ionic pathways similar to the self-assembled monolayer but to extend the concept into three dimensions. The challenge will be to control the assembly of the crystals such that the COOH layers are large enough to provide a continuous ion pathway over a relevant length scale and are oriented in useful directions. The AR structure is expected to be superior to the EC structure for ion transport because in the EC structure the layers of carboxyl groups share the layer plane with hydrophobic methylene and methine groups, which could impede the ion pathways. The presence of these hydrophobic groups also dilutes the areal density of carboxyl groups, which is only 3.1 nm^{-2} in the EC2 simulation. For transport purposes, alignment of the layered structures is desired, and such alignment can be achieved via mechanical deformation[20] and perhaps via directed self-assembly.

5. CONCLUSION

The layered morphology of an ADMET PE with carboxylic acid groups pendant from every 21st carbon atom was studied in detail using atomistic MD simulations, X-ray scattering, and Raman spectroscopy. We find that the simulated adjacent-reentry structure matches the experimental data obtained from a melt-crystallized sample. The stereoirregular adjacent-reentry simulation matched both the low-q and high-q experimental X-ray scattering data. The experimental Raman spectrum shows hexagonal packing of mostly trans alkyl segments. This agrees well with experimental X-ray scattering and the packing observed in the stereoirregular simulations.

The intriguing advantage of the adjacent-reentry morphology is the presence of layered channels of the functional groups. This remarkable morphology might facilitate rapid transport within these layers, independent of the polymer segmental dynamics. Optimal transport will rely on judicious selection of the pendant group chemistry. Our preliminary results with a semicrystalline precise sulfonic-acid-containing PE show excellent conductivity that could be even further improved by fabricating a macroscopically anisotropic layered morphology.

■ ASSOCIATED CONTENT

ⓈSupporting Information

The Supporting Information is available free of charge on the ACS Publications website at DOI: 10.1021/jacs.6b12817.

> Experimental and simulation methods; final energies, energetic components, and densities of all simulations; additional snapshots of EC simulations; distribution of backbone dihedral angles; additional snapshots of AR

simulations; structure factor of PE simulation; Raman fits (PDF)

■ AUTHOR INFORMATION

Corresponding Author
*winey@seas.upenn.edu

ORCID Ⓘ
Edward B. Trigg: 0000-0002-4723-650X

Notes
The authors declare no competing financial interest.

■ REFERENCES

(1) Schulz, M. D.; Wagener, K. B. *Macromol. Chem. Phys.* **2014**, *215*, 1936−1945.

(2) Atallah, P.; Wagener, K. B.; Schulz, M. D. *Macromolecules* **2013**, *46*, 4735−4741.

(3) Baughman, T. W.; Chan, C. D.; Winey, K. I.; Wagener, K. B. *Macromolecules* **2007**, *40*, 6564−6571.

(4) Berson, J.; Burshtain, D.; Zeira, A.; Yoffe, A.; Maoz, R.; Sagiv, J. *Nat. Mater.* **2015**, *14*, 613−621.

(5) Hallinan, D. T., Jr; Balsara, N. P. *Annu. Rev. Mater. Res.* **2013**, *43*, 503−525.

(6) Cheng, S.; Smith, D. M.; Pan, Q.; Wang, S.; Li, C. Y. *RSC Adv.* **2015**, *5*, 48793−48810.

(7) Sadoway, D. R.; Huang, B.; Trapa, P. E.; Soo, P. P.; Bannerjee, P.; Mayes, A. M. *J. Power Sources* **2001**, *97-98*, 621−623.

(8) Aurbach, D.; Talyosef, Y.; Markovsky, B.; Markevich, E.; Zinigrad, E.; Asraf, L.; Gnanaraj, J. S.; Kim, H.-J. *Electrochim. Acta* **2004**, *50*, 247−254.

(9) Xue, Z.; He, D.; Xie, X. *J. Mater. Chem. A* **2015**, *3*, 19218−19253.

(10) Thomas, K. E.; Sloop, S. E.; Kerr, J. B.; Newman, J. *J. Power Sources* **2000**, *89*, 132−138.

(11) Gadjourova, Z.; Andreev, Y. G.; Tunstall, D. P.; Bruce, P. G. *Nature* **2001**, *412*, 520−523.

(12) Stoeva, Z.; Martin-Litas, I.; Staunton, E.; Andreev, Y. G.; Bruce, P. G. *J. Am. Chem. Soc.* **2003**, *125*, 4619−4626.

(13) Cheng, S.; Smith, D. M.; Li, C. Y. *Macromolecules* **2014**, *47*, 3978−3986.

(14) O'Gara, J. E.; Wagener, K. B.; Hahn, S. F. *Makromol. Chem., Rapid Commun.* **1993**, *14*, 657−662.

(15) Berda, E. B.; Wagener, K. B. *Mater. Sci. Technol.* **2013**, 587−600.

(16) Lieser, G.; Wegner, G.; Smith, J. A.; Wagener, K. B. *Colloid Polym. Sci.* **2004**, *282*, 773−781.

(17) Santonja-Blasco, L.; Zhang, X.; Alamo, R. G. *Adv. Polym. Sci.* **2015**, *276*, 133−182.

(18) Boz, E.; Wagener, K. B.; Ghosal, A.; Fu, R.; Alamo, R. G. *Macromolecules* **2006**, *39*, 4437−4447.

(19) Buitrago, C. F.; Jenkins, J. E.; Opper, K. L.; Aitken, B. S.; Wagener, K. B.; Alam, T. M.; Winey, K. I. *Macromolecules* **2013**, *46*, 9003−9012.

(20) Middleton, L. R.; Szewczyk, S.; Azoulay, J.; Murtagh, D.; Rojas, G.; Wagener, K. B.; Cordaro, J.; Winey, K. I. *Macromolecules* **2015**, *48*, 3713−3724.

(21) Buitrago, C. F.; Jenkins, J. E.; Opper, K. L.; Aitken, B. S.; Wagener, K. B.; Alam, T. M.; Winey, K. I. *Macromolecules* **2013**, *46*, 9003−9012.

(22) Hosoda, S.; Nozue, Y.; Kawashima, Y.; Utsumi, S.; Nagamatsu, T.; Wagener, K.; Berda, E.; Rojas, G.; Baughman, T.; Leonard, J. *Macromol. Symp.* **2009**, *282*, 50−64.

(23) Hosoda, S.; Nozue, Y.; Kawashima, Y.; Suita, K.; Seno, S.; Nagamatsu, T.; Wagener, K. B.; Inci, B.; Zuluaga, F.; Rojas, G.; Leonard, J. K. *Macromolecules* **2011**, *44*, 313−319.

(24) Rojas, G.; Inci, B.; Wei, Y.; Wagener, K. B. *J. Am. Chem. Soc.* **2009**, *131*, 17376−17386.

(25) Holmes, D.; Bunn, C.; Smith, D. *J. Polym. Sci.* **1955**, *17*, 159−177.

(26) Inoue, K.; Hoshino, S. *J. Polym. Sci., Polym. Phys. Ed.* **1973**, *11*, 1077−1089.

(27) Kaner, P.; Ruiz-Orta, C.; Boz, E.; Wagener, K. B.; Tasaki, M.; Tashiro, K.; Alamo, R. G. *Macromolecules* **2014**, *47*, 236−245.

(28) Tasaki, M.; Yamamoto, H.; Hanesaka, M.; Tashiro, K.; Boz, E.; Wagener, K. B.; Ruiz-Orta, C.; Alamo, R. G. *Macromolecules* **2014**, *47*, 4738−4749.

(29) Gaines, T. W.; Trigg, E. B.; Winey, K. I.; Wagener, K. B. *Macromol. Chem. Phys.* **2016**, *217*, 2351−2359.

(30) Chanda, S.; Ramakrishnan, S. *Macromolecules* **2016**, *49*, 3254−3263.

(31) Roy, R. K.; Gowd, E. B.; Ramakrishnan, S. *Macromolecules* **2012**, *45*, 3063−3069.

(32) Wentzel, N.; Milner, S. T. *J. Chem. Phys.* **2010**, *132*, 044901.

(33) Rastogi, S.; Kurelec, L.; Lemstra, P. J. *Macromolecules* **1998**, *31*, 5022−5031.

(34) Peacock, A. *Handbook of Polyethylene: Structures, Properties, and Applications*; Marcel Dekker: New York, 2000.

(35) Kurelec, L.; Rastogi, S.; Meier, R.; Lemstra, P. *Macromolecules* **2000**, *33*, 5593−5601.

(36) Boerio, F. J.; Koenig, J. L. *J. Chem. Phys.* **1970**, *52*, 3425−3431.

(37) Migler, K. B.; Kotula, A. P.; Hight Walker, A. R. *Macromolecules* **2015**, *48*, 4555−4561.

(38) Meier, R. J. *Polymer* **2002**, *43*, 517−522.

(39) Jenkins, J. E.; Seitz, M. E.; Buitrago, C. F.; Winey, K. I.; Opper, K. L.; Baughman, T. W.; Wagener, K. B.; Alam, T. M. *Polymer* **2012**, *53*, 3917−3927.

(40) Lee, K.-S.; Wegner, G.; Hsu, S. L. *Polymer* **1987**, *28*, 889−896.

(41) Strobl, G.; Hagedorn, W. *J. Polym. Sci., Polym. Phys. Ed.* **1978**, *16*, 1181−1193.

(42) Zhao, Y. H.; Abraham, M. H.; Zissimos, A. M. *J. Org. Chem.* **2003**, *68*, 7368−7373.

(43) Middleton, L. R.; Trigg, E. B.; Schwartz, E.; Opper, K. L.; Baughman, T. W.; Wagener, K. B.; Winey, K. I. *Macromolecules* **2016**, *49*, 8209−8218.